Inertial and geometrical effects of self-propelled elliptical Brownian particles

Inertial and geometrical effects of self-propelled elliptical Brownian particles

Federica Montana
Department of Mathematical Sciences, Politecnico di Torino, Turin, Italy and INFN, Sezione di Torino, Turin, Italy

Carlo Camporeale
Department of Environmental, Land and Infrastructure Engineering, Politecnico di Torino, Turin, Italy

Amilcare Porporato
Department of Civil and Environmental Engineering, Princeton University, Princeton, New Jersey, USA and High Meadows Environmental Institute, Princeton University, Princeton, New Jersey, USA

Lamberto Rondoni
Department of Mathematical Sciences, Politecnico di Torino, Turin, Italy and INFN, Sezione di Torino, Turin, Italy

(Received 15 February 2023; accepted 11 May 2023; published 31 May 2023)

Active particles that self-propel by transforming energy into mechanical motion represent a growing area of research in mathematics, physics, and chemistry. Here we investigate the dynamics of nonspherical inertial active particles moving in a harmonic potential, introducing geometric parameters which take into account the role of eccentricity for nonspherical particles. A comparison between the overdamped and underdamped models for elliptical particles is performed. The model of overdamped active Brownian motion has been used to describe most of the basic aspects of micrometer-sized particles moving in a liquid ("microswimmers"). We consider active particles by extending the active Brownian motion model to incorporate translation and rotation inertia and account for the role of eccentricity. We show how the overdamped and the underdamped models behave in the same way for small values of activity (Brownian case) if eccentricity is equal to zero, but increasing eccentricity leads the two dynamics to substantially depart from each other—in particular, the action of a torque induced by external forces, induced a marked difference close to the walls of the domain if eccentricity is high. Effects induced by inertia include an inertial delay time of the self-propulsion direction from the particle velocity, and the differences between the overdamped and underdamped systems are particularly evident in the first and second moments of the particle velocities. Comparison with the experimental results of vibrated granular particles shows good agreement and corroborates the notion that self-propelling massive particles moving in gaseous media are dominated by inertial effects.

DOI: 10.1103/PhysRevE.107.054607

I. INTRODUCTION

Active fluids consist of environments populated by self-propelled "particles" [1], such as bacteria, microtubule networks, or artificial swimmers. These differ substantially from standard fluids, made of inert particles as they are able to absorb energy from the environment and convert it into directed motion [2]. Active fluids have been experimentally and theoretically analyzed for a variety of systems, with a focus on biological or artificial microswimmers [3–6], cell colonies [6–8], or protein filaments [9]. Comprehensive reviews are reported in [2,10–12]. In all these systems, the inertial effect can be neglected as these micrometer-sized particles typically self-propel in a liquid at a very low Reynolds number. Therefore, the dynamics of these colloidal particles in a solvent are overdamped and well described by the so-called active Brownian motion [13,14].

The active Brownian particle model has been tested on experimental data on self-moving colloids [13,15,16] and has also been used to describe and predict collective phenomena in colloids and bacteria [2]. However, recent works studied larger self-propelled particles, or motion in low-density environments, where the Reynolds numbers are not small, and the consequences of inertial effects cannot be neglected [12,17,18]. Examples include the so-called "complex plasma," i.e., mesoscopic dust particles in plasmas [19], or granules brought to self-propulsion on a vibrating plate [17,20–28] or with an internal vibration motor [29]. Other examples of self-propelled particles with inertia range from minirobots [30,31] and macroscopic swimmers [32] to biological particles like beetles that can fly [33] or swim at water interfaces [34]. Many interesting applications in various domains can be developed by realizing artificial microswimmers. They can be used as autonomous agents to localize, pick up, and deliver nanoscopic objects in many applications, including drug delivery via tissues, performance in lab-on-a-chip systems, and gene therapy [35–37]. There are numerous examples of macroscopic self-propelling devices where inertia is dominant [38–43]. Most of the active particles in nature, such as bacteria, generally deviate from the ideal spherical

shape, assuming rather elliptical or more complex shapes. This, of course, modifies the swimming properties of the particles. However, the model cited so far did not fully take into account the geometry of the particles.

In the present work, the theory of Brownian motion will be the starting point to derive the underdamped Langevin formalism for the case of active Brownian particles confined by harmonic walls, such as the ones described by Solon *et al.* [44]. In order to take into account the elliptical shape of the particles, the friction and diffusion coefficients are generalized with a matrix formalism, which takes into account the correct shape and orientation of the particles. The effect of particle eccentricity is highlighted, as well as the differences between the overdamped and underdamped models.

This paper is organized as follows. In Sec. II the overdamped and underdamped models are presented: we mainly consider the case of an elliptical active Brownian particle confined by two harmonic walls. In Sec. II C the concepts of friction and diffusion coefficient are generalized to obtain friction and diffusion matrix [cf. Eqs. (17) and (18)], which take into account the elliptical shape and orientation of the particle. After scaling the variables to get dimensionless equations, stochastic simulations have been carried out and the results are presented in Sec. III. The results highlight the differences and similarities between the overdamped and the underdamped models in their particle density profiles, mean velocity and second momentum of velocity, and the role played by eccentricity. Finally, in Sec. III B the importance of inertia on macroscopic self-propelled particles is demonstrated by reproducing the experimental results of [45] and the mean-square displacement varying the value of activity and eccentricity (Fig. 8 below). We conclude with some general remarks and a few open questions in Sec. IV.

II. STOCHASTIC MODELING

A. The overdamped model

One of the most popular models of active particles is the Langevin overdamped stochastic dynamics, which has the advantage of being particularly simple, and it is also considered appropriate in the case of bacteria when their self-propulsion is not particularly strong. In this work we first consider a fluid with viscosity η and density ρ, containing noninteracting, three-dimensional ellipsoidal active Brownian particles (ABPs), which move in a two-dimensional plane of coordinates (x, y). The principal semiaxis a of the ellipsoid makes an angle $\theta(t)$ with respect to the direction of the x axis. The activity of the particles is given by a contribution to the motion of the particles that is constant, with activity coefficient v_s, and is oriented like the direction of the principal axis. Moreover, an external generalized force $\boldsymbol{K} = [\boldsymbol{F}, \boldsymbol{T}]$ acts on the system, where $\boldsymbol{F} = [F(x), F(y)]$ refers to the Cartesian components of the velocity, and $\boldsymbol{T} = \mathcal{T}(\theta)$ represents the effect of a torque on the angle θ. In the overdamped case, this amounts to the following set of equations of motion:

$$\xi \dot{x} = F_x + \xi v_s \cos\theta + \xi\sqrt{2D_t}\Gamma_x, \tag{1}$$

$$\xi \dot{y} = F_y + \xi v_s \sin\theta + \xi\sqrt{2D_t}\Gamma_y, \tag{2}$$

$$\xi_r \dot{\theta} = \mathcal{T}(\theta) + \xi_r\sqrt{2D_r}\Gamma_\theta, \tag{3}$$

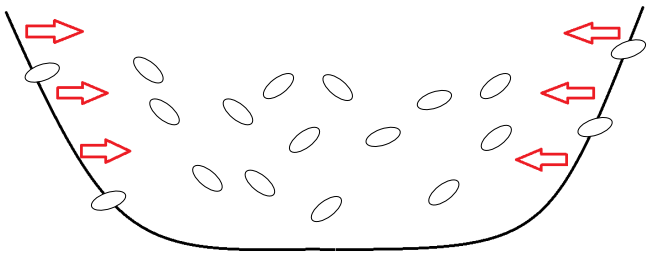

FIG. 1. Sketch of the system: elliptical particles confined along the x direction by two harmonic walls.

where (F_x, F_y) is derived from a potential U, $\mathcal{T}(\theta)$ is the effect of the torque, D_t and D_r are diffusivities in space and angle, respectively, and ξ and ξ_r are the coefficients for translational and rotational friction, respectively. This model is considered in Ref. [44], mainly with $F_y = 0$ and F_x given by a harmonic confining potential,

$$U(x) = \frac{\lambda}{2}\Theta[x - x_w](x - x_w)^2, \tag{4}$$

where Θ is the Heaviside function and x_w is the wall position. In this way, we will consider a system of particles moving within a channel of given width, which was also the subject of numerous works (Fig. 1); see, e.g., Refs. [18,46,47]. If particles are elongated, as in the ellipsoidal case, the torque produced by the confining potential is expressed by

$$\mathcal{T}(\theta) = \lambda\kappa\Theta[x - x_w]\sin 2\theta, \tag{5}$$

with $\kappa = (a^2 - b^2)/8$, $\xi = 6\pi a\eta$, $\xi_r = 8\pi a^3\eta$, and $D_t = k_B T_b/\xi$, $D_r = k_B T_b/\xi_r$. The equations of this overdamped model are recast here in the following vector form:

$$\dot{\boldsymbol{x}} = \boldsymbol{\xi}^{-1}\boldsymbol{K} + v_s\mathbf{n} + \sqrt{2\boldsymbol{D}}\boldsymbol{\Gamma}, \tag{6}$$

where $\mathbf{n} := \{\cos\theta, \sin\theta, 0\}$, $\boldsymbol{\xi} = \mathrm{diag}\{\xi, \xi, \xi_r\}$ and

$$\boldsymbol{K} = [-\partial_x U(x), 0, \mathcal{T}(\theta)]. \tag{7}$$

B. The underdamped model

In the case that inertial effects cannot be neglected, because of nonnegligible mass and/or propulsion mechanisms (see, e.g., Refs. [9,12,29,45,48–57]), a suitable underdamped model can be considered. Accordingly, with m the mass of the particles and J the moment of inertia per unit mass, the underdamped version of the model described above is expressed by the following set of equations:

$$\dot{x} = v_x\,, \quad \dot{y} = v_y\,, \quad \dot{\theta} = v_\theta, \tag{8}$$

$$\dot{v}_x = -\frac{1}{m}F(x) + \gamma\, v_s\cos(\theta) - \gamma v_x + \sqrt{2D_x}\Gamma_x\,, \tag{9}$$

$$\dot{v}_y = \gamma\, v_s\sin(\theta) - \gamma v_y + \sqrt{2D_y}\Gamma_y\,, \tag{10}$$

$$\dot{v}_\theta = \frac{\mathcal{T}(\theta)}{m\sqrt{J}} - \gamma_\theta v_\theta + \sqrt{2D_\theta}\Gamma_\theta, \tag{11}$$

where $J = (a^2 + b^2)/5$ for an elliptical particle, $\tau_v = (6\pi a\eta/m)^{-1} = \gamma^{-1}$ gives the viscous timescale, $\gamma_\theta = \xi_r/mJ$ [45], and the angular variables have been scaled replacing θ

with $\theta J^{1/2}$. This latter scaling allows the set of equations to be dimensionally homogenous. The result is that the two-dimensional motion of the rotating objects is formally equivalent to a three-dimensional random walk of a point particle, with periodic boundary conditions along one direction. The vector form of Eqs. (9)–(11) reads

$$\ddot{\boldsymbol{x}} = \frac{\boldsymbol{K}}{m} + \gamma(v_s \mathbf{n} - \boldsymbol{G}\dot{\boldsymbol{x}}) + \sqrt{2\boldsymbol{D}}\boldsymbol{\Gamma}, \tag{12}$$

where $\boldsymbol{x} := (x, y, \theta)$,

$$\boldsymbol{K} = (-\partial_x U(\boldsymbol{x}), 0, \mathcal{T}(\theta/\sqrt{J})), \tag{13}$$

and

$$\boldsymbol{G} = \begin{pmatrix} \gamma & 0 & 0 \\ 0 & \gamma & 0 \\ 0 & 0 & \gamma_\theta \end{pmatrix}; \quad \boldsymbol{D} = D_x \begin{pmatrix} 1 & 0 & 0 \\ 0 & 1 & 0 \\ 0 & 0 & \alpha \end{pmatrix} \tag{14}$$

with

$$D_x = \frac{kT_b\gamma}{m}, \quad D_\theta = D_r\gamma_\theta^2 J, \quad \alpha = \frac{D_\theta}{D_x}.$$

The "temperature" T_b is to be properly understood. It represents a reservoir of energy contributing to the random motion of the particles. As in granular fluids and other dissipative systems made of particles much larger than the atomic scales, T_b is an *effective* temperature, in the sense that it plays a role analogous to that of the bath temperature in equilibrium systems. Even if in thermal equilibrium with their fluid, particles such as bacteria would not be influenced by the thermal fluctuations of the fluid. In general, their "kinetic temperature" (obtained applying the energy equipartition principle to their kinetic energy) would differ from the thermodynamic one.

Note also that the system (8)–(11) reduces to the overdamped case [(1)–(3)] in the $m \to 0$ limit, as detailed in Appendix A. However, this does not immediately imply that the solutions of the first set of equations converge to the solutions of the second one, since such kinds of limits are typically singular. In fact, it is known that in certain cases the small inertia limit of underdamped Langevin equations does not reproduce the corresponding overdamped dynamics [58]. A comparison of the overdamped with the underdamped model is interesting also from this point of view.

C. Physical remarks on the matrices *G* and *D*

A more realistic form of the tensors $\boldsymbol{G}$ and $\boldsymbol{D}$ can be deduced on physical grounds. First, it is clear that $\boldsymbol{G}$ has nonvanishing off-diagonal elements if the geometry is not spherical. This aspect is usually neglected in the literature [44,45], although the drag on nonspherical bodies is a well-established fluid dynamic topic. In our case, a viscous fluid interacting with an axially symmetric body in roto-translation motion is considered [59]. Accordingly, we consider a local reference frame $(\hat{x}, \hat{y})$ corresponding to the semiaxes of our active particles, and we decompose the drag on the body into components (Fig. 2). At low Reynolds numbers and in the particle frame, the drag can be written in a Stokes-like form, corrected with two coefficients, $\sigma_\parallel$, $\sigma_\perp$ in the direction parallel and orthogonal to the main axis, respectively [60]. Likewise, rotational friction is proportional to a coefficient

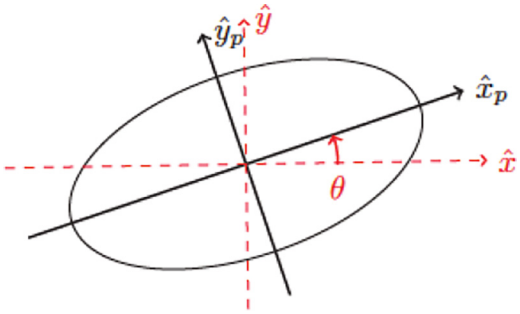

FIG. 2. Sketch of the frame of the particle. Figure is taken from Solon *et al.* [44].

$\gamma\sigma_r$. According to [61], the functions $\sigma_\parallel$ and $\sigma_\perp$ for a prolate shape read

$$\sigma_\parallel = \frac{(8/3)e^3}{(1+e^2)\log\left[\frac{1+e}{1-e}\right] - 2e},$$
$$\sigma_\perp = \frac{(16/3)e^3}{(3e^2-1)\log\left[\frac{1+e}{1-e}\right] + 2e}, \tag{15}$$

where $e = [1-(b/a)^2]^{\frac{1}{2}}$ is the eccentricity of the body. Basically, $\sigma_\parallel$ and $\sigma_\perp$ are complex functions of the body eccentricity, while σ_r is well known for the spherical case: $\sigma_r = 10/3$ [[62], p. 436]. To the best of our knowledge, no closed forms are known for σ_r in the case of rotation of a prolate spheroid around the axis orthogonal to the plane (x, y).

Let θ be the angle that the major axis of our ellipsoid makes with the direction x, at a given instant of time, while it moves with velocity $\mathbf{v}_o = (v_x, v_y)$, with respect to the (absolute) laboratory reference frame, with axes (x, y). The form of the tensor $\boldsymbol{G}$ is obtained by projecting the vector $\mathbf{v}_o$ on the local frame, computing the drag, and then returning to the absolute frame. In the laboratory frame, one then obtains the *grand resistance friction matrix* as $\boldsymbol{G} = \mathbf{R}\boldsymbol{\Sigma}\mathbf{R}^{\mathrm{T}}$, where

$$\mathbf{R} = \begin{pmatrix} \cos\theta & \sin\theta & 0 \\ \sin\theta & \cos\theta & 0 \\ 0 & 0 & 1 \end{pmatrix}, \quad \boldsymbol{\Sigma} = \begin{pmatrix} \sigma_\parallel & 0 & 0 \\ 0 & \sigma_\perp & 0 \\ 0 & 0 & \sigma_r \end{pmatrix}. \tag{16}$$

Furthermore, by introducing the rotational drag we eventually get

$$\boldsymbol{G} = \gamma \begin{pmatrix} \sigma_\parallel \cos^2\theta + \sigma_\perp \sin^2\theta & \frac{\sigma_\parallel - \sigma_\perp}{2}\sin 2\theta & 0 \\ \frac{\sigma_\parallel - \sigma_\perp}{2}\sin 2\theta & \sigma_\perp \cos^2\theta + \sigma_\parallel \sin^2\theta & 0 \\ 0 & 0 & \sigma_r \end{pmatrix}, \tag{17}$$

with $\gamma = 6\pi a\eta/m$. Therefore, the tensor has off-diagonal terms and depends on θ. Notice that, in the spherical case $(e \to 0)$ $\sigma_\parallel = \sigma_\perp = 1$, and (17) reduces to (14), with $\gamma_\theta = (10/3)\gamma$, and Stokes' law is retrieved. In the present work, the underdamped model of active particles will refer to the vector equation (12), with the nondiagonal friction matrix (17) in place of the diagonal one, (14), commonly found in the literature. This allows us to investigate the effect of eccentricity.

Concerning the third component of the tensor $\boldsymbol{D}$, which determines the noise acting on the angle θ in Eq. (11), a

direct application of the fluctuation-dissipation theorem (FDT) [63,64] allows one to set $D_x = D_y = D_0$ and $D_\theta = \alpha D_0$, where $D_0 = \gamma k T_b \sigma/m$, $\sigma = (\sigma_\parallel + \sigma_\perp)/2$, k is the Boltzman constant, and $T_b = m\sqrt{2D_t}/k_B$ is the *effective* bath temperature. The quantity α is computed according to

$$\alpha = \frac{D_\theta}{D_x} = \frac{D_r(\gamma\sigma_\theta)^2 J}{D_t(\gamma\sigma)^2} = \frac{D_r}{D_t}\left(\frac{\sigma_\theta}{\sigma}\right)^2 J. \tag{18}$$

In Appendix B, it is shown that, for thermal reasons, α has a lower bound roughly equal to 5/4, for any eccentricity. Nevertheless, active particles may increase their rotational noise, and most often α is very larger than that bound.

D. Scaling

Dimensionless versions of overdamped and underdamped models can be obtained scaling time with $\tau = D_r^{-1}$, while lengths are scaled with the size of the simulated box L, and velocities with the quantity LD_r. Therefore, after introducing the following dimensionless numbers:

$$N_1 = \frac{\lambda}{\xi D_r}, \quad N_2 = \frac{\lambda\kappa}{\xi_r D_r}, \quad N_3 = \frac{v_s}{LD_r}, \\ N_4 = \frac{\sqrt{2\sigma_r J}}{L}, \quad \sigma_r = \frac{D_t}{D_r J}, \quad R_\tau = \frac{mD_r}{\xi}, \tag{19}$$

the dimensionless overdamped equations read

$$\begin{aligned} \dot{x} &= -N_1(x-1) + N_3\cos\theta + N_4\Gamma_x, \\ \dot{y} &= N_3\sin\theta + N_4\Gamma_y, \\ \dot{\theta} &= N_2\sin 2\theta + \sqrt{2}\Gamma_\theta. \end{aligned} \tag{20}$$

The corresponding dimensionless underdamped equations are instead given by

$$\begin{aligned} R_\tau\dot{v}_x &= -N_1(x-1) + \sigma_\parallel N_3\cos\theta - G_{11}v_x + G_{22}v_y + N_4\Gamma_x, \\ R_\tau\dot{v}_y &= \sigma_\parallel N_3\sin\theta - G_{21}v_x + G_{22}v_y + N_4\Gamma_y, \\ R_\tau\dot{v}_\theta &= \sigma_r N_2\sin 2\theta - \sigma_r G_{33}v_\theta + \sigma_r\sqrt{2}\Gamma_\theta. \end{aligned} \tag{21}$$

We remark that the parameter N_3 is a sort of Péclet number, since it is the ratio between the particle velocity and a characteristic diffusive velocity LD_r. Instead R_τ is equivalent to the ratio between the characteristic timescale of the underdamped model m/ξ and the timescale of the overdamped model D_r^{-1}. It follows that R_τ is identically zero in the overdamped approach. Finally, it is straightforward to show that $N_3 R_\tau = \frac{1}{9}\frac{a}{L}\mathrm{Re}(1-e^2)^{2/3}$ where $\mathrm{Re} = \rho v_s d_{eq}/\eta$ is the *particle Reynolds number*, built with the equivalent diameter $d_{eq} = (6V/\pi)^{1/3}$, V being the particle volume, approximated with an ellipsoidal shape [65,66].

III. SIMULATIONS AND RESULTS

We simulated 5×10^5 active particles, initially randomly distributed in the interval $x \in [-2, 2]$, with initial vanishing speed and random orientation (Fig. 3). The positions $x = -1$ and $x = 1$ were the centers of (half) harmonic potentials (4) that act only on particles with $x < -1$ and $x > 1$, respectively [44]. The particles were allowed to wander in a larger domain $x \in [-3, 3]$. Periodic boundary conditions have been adopted in the y direction with a period $\Delta y = 1$. The bath effective temperature was set to 300 K, and the behavior of some "mesoscopic" quantities, such as the density distribution, and the first and the second moments of velocity were then analyzed. Following de Groot and Mazur [67], given $j = \{x, y, \theta\}$ and $n = \{1, 2\}$, the mesoscopic quantities are defined according to

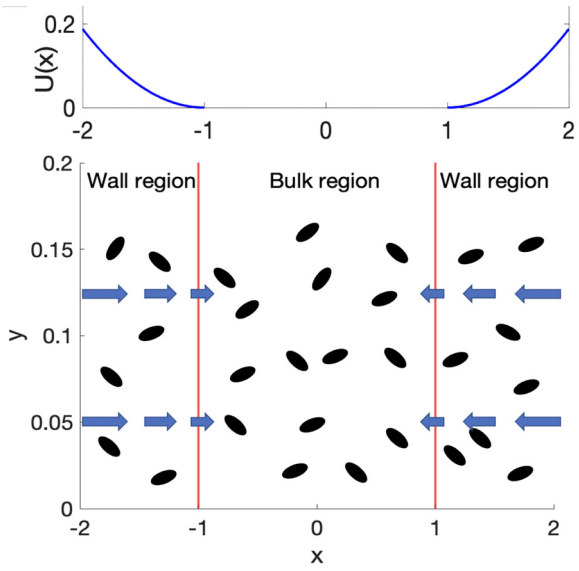

FIG. 3. The simulation box of the ABP with periodic boundary conditions in the y direction. The particles are injected in the range $x \in [-2, 2]$ and the harmonic potential (i.e., a recovering force) in blue is set for $x > 1$ and $x < -1$, thus simulating the presence of two "harmonic walls" which repel, pushing particles toward the bulk of the domain.

$$\rho(x,t) = \int dy\, d\theta\, d\dot{\boldsymbol{x}}\, p(\boldsymbol{x}, \dot{\boldsymbol{x}}, t), \tag{22}$$

$$\langle v_j^n\rangle(x,t) = \int dy\, d\theta\, d\dot{\boldsymbol{x}}\, v_j^n p(\boldsymbol{x}, \dot{\boldsymbol{x}}, t), \tag{23}$$

where $p = p(\boldsymbol{x}, \dot{\boldsymbol{x}}, t)$ is the probability distribution function for the stochastic differential equations (21). Numerically, the density and the moments of the velocity were computed by dividing the domain of interest ($x \in [-2, 2]$) in bins and then counting, for a sufficiently long time, the number of particles in every bin at each time step, normalized by the total counts.

The computation of the stationary density needs first a finite time allowing the initial uniform distribution of particles to relax to the stationary one. In our simulations, this relaxation time has been estimated as the time at which the time-dependent particle density varies in time no more than $\pm1\%$ in the L_2 norm, which is the square root of the integral of the squared difference of two functions. As commented in the following, the duration of the runs then depends on the parameters, and it differs between overdamped and underdamped dynamics.

A. Results

As expected, the overdamped dynamics reaches the stationary state much faster than the underdamped one. Moreover, for $N_3 = 0$, which corresponds to the Brownian

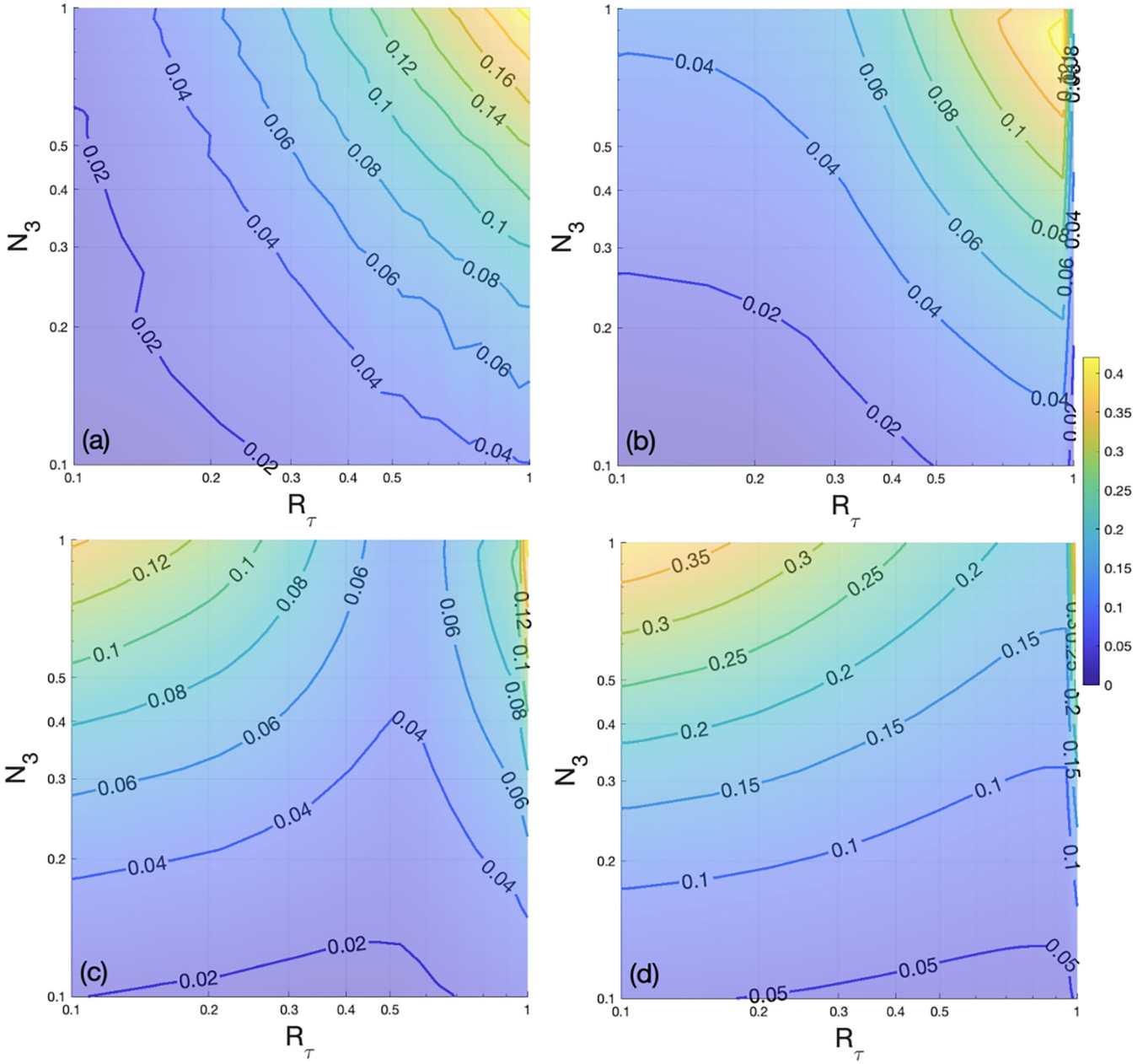

FIG. 4. Contour map of $\Delta\rho$, the difference between the overdamped and underdamped steady-state particle density profiles, as a function of the dimensionless parameter $N_3 = v_s/LD_r$ and of the ratio between the two characteristic scales $R_\tau = mD_r/\xi$. (a) $e = 0$, (b) $e = 0.45$, (c) $e = 0.67$, (d) $e = 0.9$. Axes are reported in log-log scale to emphasize small values of R_τ and N_3.

motion of passive ellipsoids, the simulation time to reach the equilibrium state can be three orders of magnitude longer than the time needed to reach a nonequilibrium stationary state with $N_3 > 0$, for both over- and underdamped dynamics. This is the case because the energy dissipation characterizing the active particles promotes convergence to a stationary state, as commonly expected [68,69].

1. Density profiles

The first observable to consider, and to check whether it differs between overdamped and underdamped cases, is the particle density profile. Here we evaluate the asymptotic L_1 norm of the difference between the respective densities ρ_o and ρ_u that arise in time starting from the same initial conditions:

$$\Delta\rho = \int_{-2}^{2} dx |\rho_u(x) - \rho_o(x)|, \tag{24}$$

where we have normalized the densities, so that

$$\int_{-2}^{2} \rho_i(x)\, dx = 1 \quad \text{with } i = o, u.$$

The results are reported in Fig. 4 for different values of the parameters R_τ and N_3, namely, different values of the inertial effects, respectively, due to the mass and to self-propulsion, and for different values of the eccentricity: $e = 0, 0.45, 0.67, 0.9$. In particular, Fig. 4(a) shows for

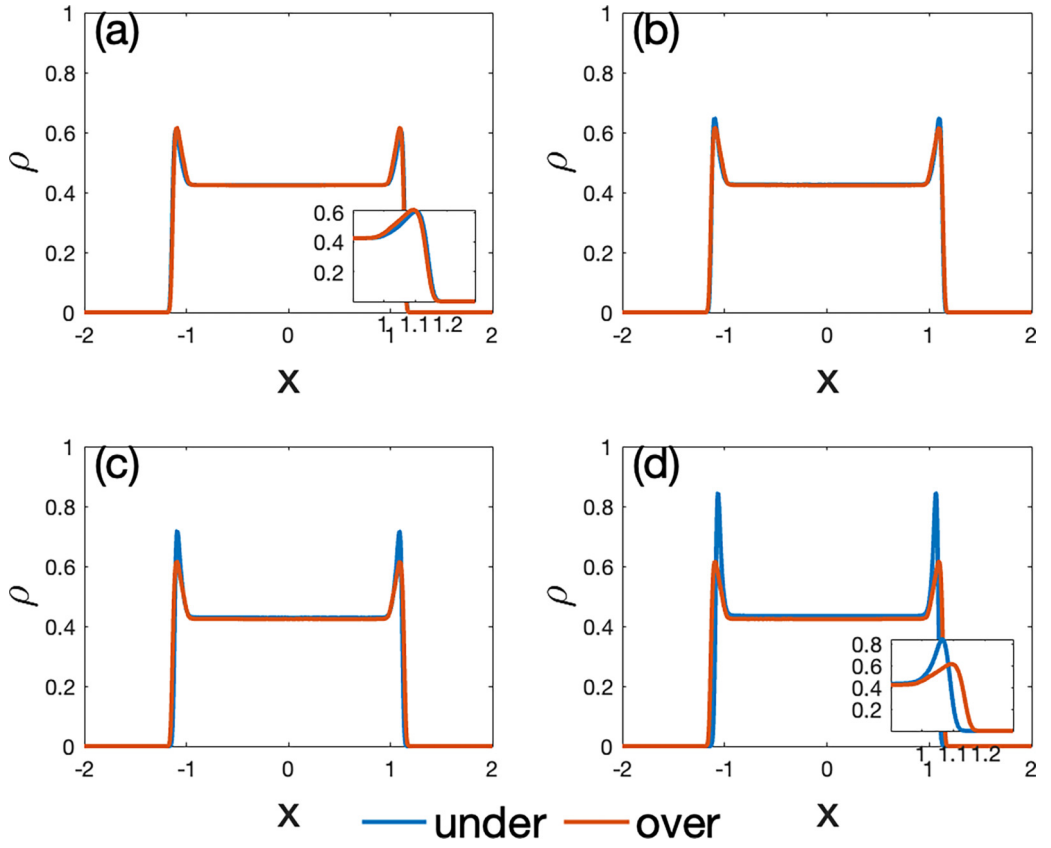

FIG. 5. Comparison between the steady-state particle density profiles of overdamped and underdamped models for different values of eccentricity. $N_3 = 0.15$ and $R_\tau = 0.15$. Eccentricity is equal to (a) 0, (b) 0.45, (c) 0.67, (d) 0.9.

spherical particles that the overdamped and the underdamped cases provide similar results for any value of N_3, when R_τ (mass effect) is negligible. Analogously, the density profiles are indistinguishable at any values of R_τ when N_3 (the propulsion, or v_s) is negligible. Hyperbolic-like contour curves—corresponding by definition to constant values of $\mathrm{Re}(1-e^2)^{2/3}$—mark the cumulative difference $\Delta\rho$, showing that the increase of either parameter or both N_3 and R_τ makes the two profiles depart from each other. As desired, the underdamped dynamics for $N_3 = 0$ and very small m reproduce the passive Brownian motion, described by overdamped equations.

The scenario changes when the eccentricity is increased. In Figs. 4(b) for $e = 0.45$, Fig. 4(c) for $e = 0.67$, and Fig. 4(d) for $e = 0.9$, the two models behave differently also at small values of N_3 and R_τ. Furthermore, one observes a qualitative change in the structure of the contour map. The hyperbolas split into two kinds, one growing and the other decreasing with R_τ. Consequently, unlike the $e = 0$ case, $\Delta\rho$ is not monotonic with R_τ and N_3. Given N_3, it first decreases and then increases with R_τ. The line of the minima of $\Delta\rho$ moves toward higher R_τ as e grows. The contour maps show that small values of N_3 allow the overdamped and underdamped models to behave in quite a similar way ($\Delta\rho < 0.05$), as evidenced also by Fig. 5. On the other hand, making the mass very small (R_τ small) important differences between the two models arise as the eccentricity grows.

Given the eccentricity of one active particle, there are two parameters, R_τ and N_3, that are independently varied in the contour map. The first gets smaller when the mass does, and the second when the activity does. We found that small mass and large activity may compensate and produce relevant inertial effects.

This suggests that, in the case of active systems, the underdamped approach is always required for highly nonspherical particles, regardless of their mass. Indeed, rotational inertia—that is influenced by eccentricity—sensibly affects the timescale of tumbling, influencing the propulsion direction.

As an example of the above arguments, Fig. 5 shows the density distributions corresponding to the case $N_3 = 0.15$ and $R_\tau = 0.15$, for different eccentricities. For $e = 0$, Fig. 5(a) shows that underdamped and overdamped models lead to approximately the same density profile. For $e = 0.45$, Fig. 5(b) reveals a small difference in the wall region, the one affected by the harmonic potential (see inset), which becomes larger and larger as the eccentricity grows. The reason is that eccentric particles accumulate near the walls of the container more than spherical particles do. The particles reaching the walls slow down, revert their velocity and gradually accelerate to return to the bulk. However, eccentric particles tend to turn parallel to the walls because the torque is applied to them, and this torque is more intense for higher eccentricity. Due to the effect of torque close to the wall, even light—but eccentric—particles oppose the motion in the direction perpendicular to their major axis, enhancing the inertial effect. Such behavior at the walls has been observed by others [46,47].

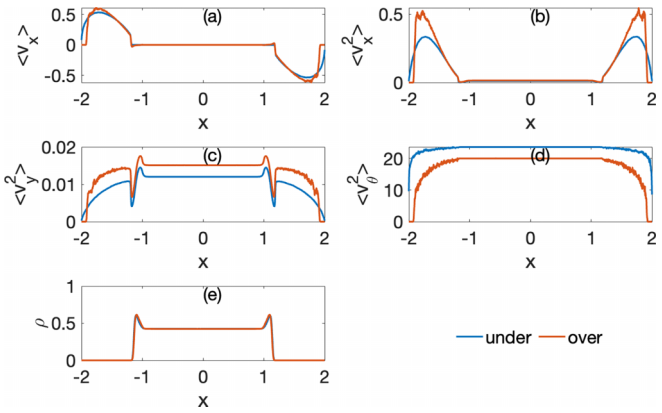

FIG. 6. (a) $\langle v_x \rangle$ is the mean velocity in the x direction, (b) $\langle v_x^2 \rangle$ is the second moment of velocity in the x direction, (c) $\langle v_y^2 \rangle$ is the second moment of velocity in the y direction, and (d) $\langle v_\theta^2 \rangle$ is the second moment of velocity in the θ direction. The density profile is reported in (e). $N_3 = 0.15$, $R_\tau = 0.15$, and $e = 0$.

2. *Ensemble-averaged particle velocities*

The differences between the overdamped and underdamped systems are particularly evident in the first and second moments of the particle velocities. Since the mean velocity in the y direction is null by construction, we will focus on $\langle v_x \rangle$, $\langle v_x^2 \rangle$, $\langle v_y^2 \rangle$, and $\langle v_\theta^2 \rangle$. It is remarkable that although overdamped and underdamped models perform similarly with respect to the density, when $e = 0$, the moments of the velocities are different (Fig, 6). This suggests again that the overdamped approximation is not sufficiently accurate in general, and the underdamped model is to be preferred. This is further evidenced by Fig. 7, which shows the effect of eccentricity on the second moment of velocity in both the overdamped model (left column), and underdamped model (right column). One observes that the overdamped model is not sensitive to variations of e [Figs. 7(a)–7(c)]. On the contrary, the underdamped model sensibly changes with e varying from 0 to 0.9 [Figs. 7(b)–7(f)].

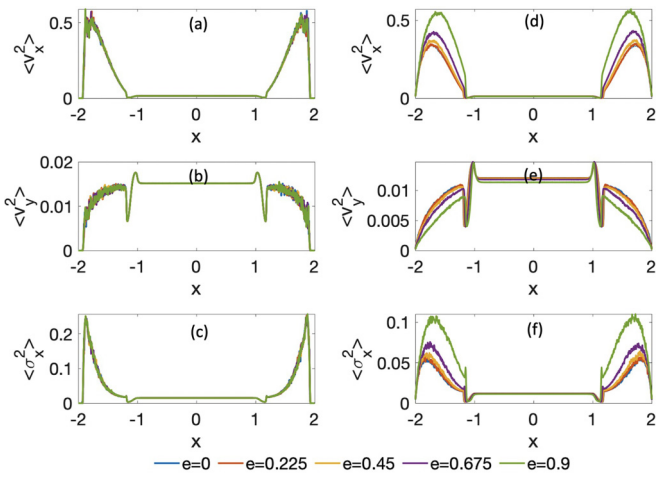

FIG. 7. Comparison between the second moment of velocity and the variance of the overdamped (a)–(c) and underdamped model (d)–(f) for different values of eccentricity $e = 0, 0.45, 0.67, 0.9$. $N_3 = 0.15$ and $R_\tau = 0.15$.

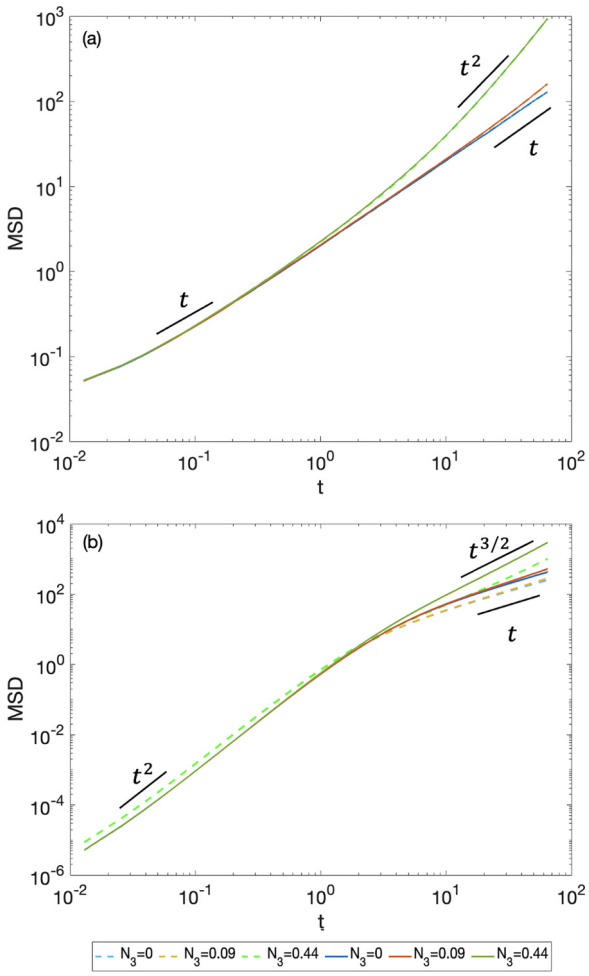

FIG. 8. Mean-square displacement as a function of time for the overdamped (a) and the underdamped case (b) for gradual increase of self-velocity and different values of eccentricity $e = 0$ (dashed lines) and $e = 0.9$ (straight lines).

3. *Diffusion processes*

Mean-square displacement (MSD $= \langle x^2 + y^2 \rangle$), is essential to understand the diffusive character of the dispersion of active nonspherical particles and how they differ from Brownian behavior. We simulated 30 000 particles, all injected in the origin of the axes, in an open axially symmetric domain, with no torque or external forces. We considered four different values of self-velocity, corresponding to $N_3 = 0, 0.09, 0.44$, and two different values of eccentricity (dashed line for $e = 0$ and a straight line for $e = 0.9$). Figure 8 shows the results of both the overdamped [Fig. 8(a)] and the underdamped [Fig. 8(b)] case. It is evident that the mean-square displacement of active particles, at a short time, has an initial diffusive behavior in the overdamped regime and a ballistic behavior in the underdamped case, in agreement with the literature [2,45,70,71]. This initial regime is independent of self-velocity.

At a longer time, the mean-square displacement may either display a diffusive regime, as happens for the passive case

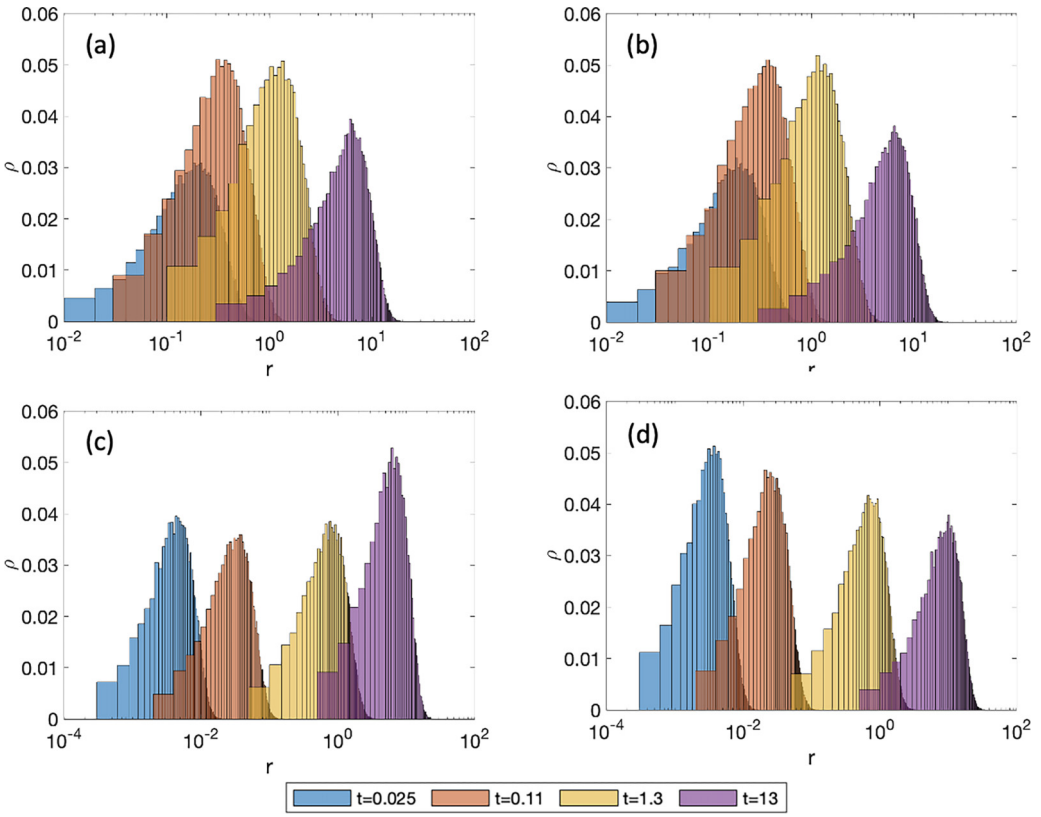

FIG. 9. Density clouds ρ as functions of the distance r from the origin of the axes, at different times $t = 0.025, 0.11, 1.3, 13$, in a log-linear plot. (a), (b) Overdamped model; (c), (d) underdamped model. Eccentricity: $e = 0$ (a), (c); $e = 9$ (b), (d).

(blue lines) or superdiffusive case, nearly parallel and very close to ballistic, for very large values of the activity [72,73]. The appearance of a superdiffusive regime in the MSD also suggests the nonequilibrium nature of the motion [70,71,74].

Figure 8 confirms the significance of the underdamped model in taking into account the role of eccentricity [Fig. 8(b)]. In fact, dashed ($e = 0$) and solid ($e = 0.9$) lines separate as the eccentricity changes. On the contrary, the overdamped system is not sensitive to variations of the geometry of the particle considered, as also shown in Fig. 7.

Finally, in order to assess the dispersion process, the space-time evolution of the density distribution has been assessed (Fig. 9). As expected, when time increases, the density clouds cover a region of space farther and farther away from the origin, where they were initially injected at $t = 0$. This is expected, but, unlike the overdamped case, the underdamped model reveals that the eccentricity has a strong impact on this behavior. To the best of our knowledge, this is a novel finding.

B. Comparison with previous experiments

In this section we adapt the stochastic simulations to reproduce the experimental results of Ref. [45]. In that work, the authors analyzed self-propelling vibrobots, and reported distinct inertial delay between particle orientation and velocity. Test particles are three-dimensionally printed vibrobots propelled by sinusoidal vibrations generated by an electromagnetic shaker. The excitation frequency and amplitude were fixed to $f = 80$ Hz and $A = 66\,\mu$m, respectively, which ensures a stable motion of the particles. The original device by Scholz *et al.* [45] is shown in Fig. 10.

Vibrobots are driven by the repeated impacts between their tilted elastic legs and a vibrating surface (so-called ratcheting mechanism). The microscopic surface inhomogeneities and a bouncing ball instability cause the particle's legs to jump asynchronously and a very irregular precession. This results in random tumbling. The leg inclination, mass, and moment of inertia of the particles were changed to explore a wide range of parameter combinations (see Table I). It has been seen from experiments that massive particles do not move instantly, but

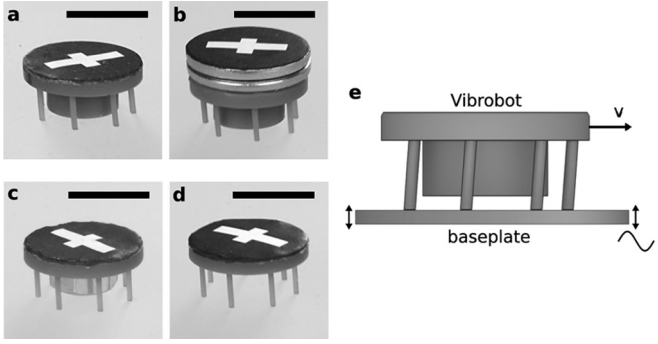

FIG. 10. 3D printed particles: (a) generic particle; (b) carrier particle with an additional outer mass; (c) tug particle with an additional central mass; (d) ring particle without a central core; (e) illustration of the mechanism of a generic particle moving on a vibrating plate. Modified from [45].

TABLE I. Mass, moment of inertia, and model parameters used in [45].

Particle	M [kg]	J [kg m^2]	V_p [m s^{-1}]	τ^{-1} [s^{-1}]	D [m^2 s^{-1}]	D_r [rad^2 s^{-1}]	τ_r^{-1} [s^{-1}]	ω_p [rad s^{-1}]
Generic	0.76×10^{-3}	1.64×10^{-8}	0.071	9.3	3.56×10^{-5}	0.91	14.9	0.354
Carrier	4.07×10^{-3}	1.46×10^{-7}	0.0929	6.85	7.7×10^{-5}	2.7	5.1	0.714
Tug	1.57×10^{-3}	2.54×10^{-8}	0.087	3.0	2.2×10^{-4}	0.59	17.6	−0.614
Ring	0.33×10^{-3}	1.26×10^{-8}	0.057	5.0	8.4×10^{-5}	2.4	5.0	−0.19

rather accelerate from rest when the vibration begins. Further details are reported in Scholz *et al.* [45].

Despite the complex nonlinear dynamics of vibrobots, Scholz's observations can be fully described by a generalized active Langevin motion model, with explicit inertial forces. Since typical particles are not perfectly symmetrical, they tend to perform circular motions on intermediate timescales. To this aim, Scholz considered an external torque τ_0, in order to drive a circular motion with average angular velocity $\omega = \tau_0/\xi_r$. This corresponds to replacing the torque introduced in (5) with τ_0. The harmonic confining potential vanishes in this case. The underdamped Langevin equations (9)–(11) therefore take the following form:

$$\dot{v}_x = \gamma\ v_s \cos(\theta) - \gamma v_x + \sqrt{2D_x}\Gamma_x, \tag{25}$$

$$\dot{v}_y = \gamma\ v_s \sin(\theta) - \gamma v_y + \sqrt{2D_y}\Gamma_y, \tag{26}$$

$$\dot{v}_\theta = \frac{\tau_0}{mJ} - \gamma_\theta v_\theta + \sqrt{2D_\theta}\Gamma_\theta. \tag{27}$$

Figure 11 displays the ensemble average of the initial velocity for four different types of particles with respect to time. Our simulations were performed using $N = 5000$ particles and are referred to a very short initial time (2 sec), with a step of $dt = 0.0001$ sec. The comparison with the experimental results reported in Fig. 2 of [45] is fairly good, which is further proof that self-propelling massive particles moving in the gaseous medium are dominated by inertial effects.

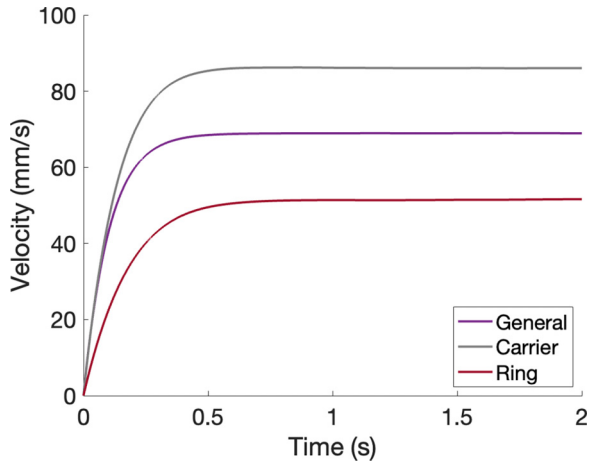

FIG. 11. Inertial delay in particle trajectories. Time dependence of the average particle velocity starting from rest at t_0 for three types of particles: generic, carrier, and ring. To compare our simulations with the experiments by Scholz, we adopted the values provided in Ref. [45] (see also the values reported in Table I), where $\tau_r = \xi_r/J$ is the rotational diffusion rate.

IV. CONCLUSIONS

We have developed a stochastic theory that highlights the role of activity, inertia, and eccentricity of nonspherical active particles. First, we have added translation and rotation inertia to common models of active Brownian motion. Then we have introduced geometric parameters which take into account the role of eccentricity for nonspherical particles, and we discuss the appropriate form and relation of the inertia tensor and diffusion matrix; cf. Sec. II C. In this regard, we evidenced the differences between overdamped and underdamped models, at different eccentricities, which turn out to be important for relatively massive particles or for large Reynolds numbers. In particular, we observed that the overdamped and the underdamped models behave in the same way for small values of activity (Brownian case) if eccentricity is equal to zero, but increasing eccentricity leads the two dynamics to substantially depart from each other. The action of a torque induced by external forces induced a marked difference close to the walls of the domain if eccentricity is high. We illustrated some effects induced by inertia, including an inertial delay time of the self-propulsion direction from the particle velocity.

This allowed us to correctly describe the experiment of Ref. [45]; a comparison of the underdamped model with data on vibrated granulars showed a good agreement between the two.

Future work will extend the present models by considering the tumbling of active particles, mathematically modelled by a Poisson shot noise term, or adding interactions between pairs of active particles. In this case, the velocity fluctuates as in an Ornstein-Uhlenbeck process, changing the direction and amplitude as particles collide with each other, at least as long as the concentration is not so high that collective phenomena emerge. Further extensions will include the role of inertia on the formation of distinct phases in the underdamped case, particularly in terms of local ordering of active particles and cluster formation.

APPENDIX A: FROM UNDERDAMPED TO OVERDAMPED MODEL

We show here how to derive the overdamped model from the underdamped Langevin equations, in the limit $m \to 0$. Let us consider the underdamped equations:

$$\dot{v}_x = -\frac{1}{m}\partial_x U(x) + \gamma\ v\cos\theta - \gamma v_x + \sqrt{2D_x}\Gamma_x, \tag{A1}$$

$$\dot{v}_y = \gamma\ v\sin\theta - \gamma v_y + \sqrt{2D_y}\Gamma_y, \tag{A2}$$

$$\dot{v}_\theta = -\frac{\mathcal{T}(\theta)}{m\sqrt{J}} - \gamma_\theta v_\theta + \sqrt{2D_\theta}\Gamma_\theta, \tag{A3}$$

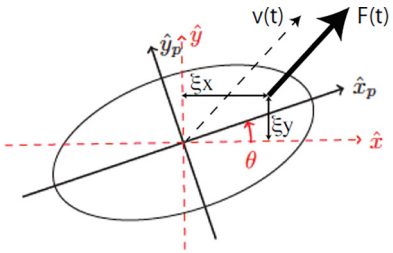

FIG. 12. Sketch of the random force acting on the elliptic particle.

with $\gamma = \xi/m$ and $D_x = \xi^2 D_t/m^2$ as in [44,45]. We get

$$m\dot{v}_x = -\partial_x U(x) + \xi\ v\cos\theta - \xi v_x + \xi\sqrt{2D_t}\Gamma_x, \quad \text{(A4)}$$

$$m\dot{v}_y = \xi\ v\sin\theta - \xi v_y + \xi\sqrt{2D_t}\Gamma_y. \quad \text{(A5)}$$

Replacing $\theta\sqrt{J}$ with θ, and letting $m \to 0$, we get

$$\xi v_x = -\partial_x U(x) + \xi\ v\cos(\theta) + \xi\sqrt{2D_t}\Gamma_x, \quad \text{(A6)}$$

$$\xi v_y = \xi\ v\sin(\theta) + \xi\sqrt{2D_t}\Gamma_y, \quad \text{(A7)}$$

which are the overdamped equations (1) and (2). Equation (A3) can be treated analogously, taking $D_\theta = \xi_r^2 D_r/m^2 J$, $\gamma_\theta = \xi_r/mJ$, θ in place of $\theta\sqrt{J}$, and $\sqrt{J}v_\theta$ in place of v_θ, we obtain

$$\sqrt{J}\ \dot{v}_\theta = \frac{\mathcal{T}(\theta)}{m\sqrt{J}} - \frac{\xi_r}{mJ}\sqrt{J}v_\theta + \frac{\xi_r}{m\sqrt{J}}\sqrt{2D_r}\Gamma_\theta. \quad \text{(A8)}$$

Multiplying for $m\sqrt{J}$ it follows that

$$mJ\ \dot{v}_\theta = \mathcal{T}(\theta) - \xi_r v_\theta + \xi_r\sqrt{2D_r}\Gamma_\theta. \quad \text{(A9)}$$

In the overdamped limit $m \to 0$ we finally obtain

$$\xi_r v_\theta = \mathcal{T}(\theta) + \xi_r\sqrt{2D_r}\Gamma_\theta, \quad \text{(A10)}$$

which is the overdamped equation (3).

APPENDIX B: FURTHER CONSIDERATIONS ABOUT THE COEFFICIENT α

A mechanistic approach allows deriving the rotational noise from the translational one [75]. In fact, physically speaking, the noise that induces a rotation of the object is equal to the torque generated by the sum of all the random collisions on the surface occurring at the same instant. Since all the noises here considered are white and reciprocally uncorrelated, we can take, without loss of generality, $\theta = 0$. The same ensemble of collisions also generates the random force having the components $\sqrt{2D_t}(\Gamma_x, \Gamma_y)$. It follows that the random torque per unit mass $\mathcal{I}$ reads

$$\mathcal{I} = a\sqrt{2D_t}(\Gamma_y\xi_x - \Gamma_x\xi_y), \quad \text{(B1)}$$

where (ξ_x, ξ_y) are the coordinates of the point of application of the random force (made here dimensionless through a for convenience). It is worth stressing that ξ_y and ξ_y are non-Gaussian random quantities which are independent of the values (Γ_x, Γ_y) since the point of application is uniformly distributed within the area of the ellipse (Fig. 12). Therefore, $\mathcal{I}$ is uncorrelated from (Γ_x, Γ_y); that is, incidentally, the reason why we can focus on the case $\theta = 0$ only. By considering the equation of the ellipse in the plane (x, y), the pdfs of these two new random variables read, respectively:

$$p_x(\xi_x) = \frac{2}{\pi}\sqrt{1-x^2}, \quad p_y(\xi_y) = \frac{2}{(1-e^2)\pi}\sqrt{1-e^2-y^2}. \quad \text{(B2)}$$

From the above considerations, one would expect to replace the last term of (11) with the quantity $\mathcal{I}/\sqrt{J}$. This would imply adding a quadratic combination of Gaussian and non-Gaussian noises into the equation. However, it is more immediate to characterize directly the random term $z(t) = \Gamma_y\xi_x - \Gamma_x\xi_y$ as a whole. To this aim, we first need the pdf of the first addend, $z_1(t) = \Gamma_y(t)\xi_x(t)$. By recalling that Γ_y is

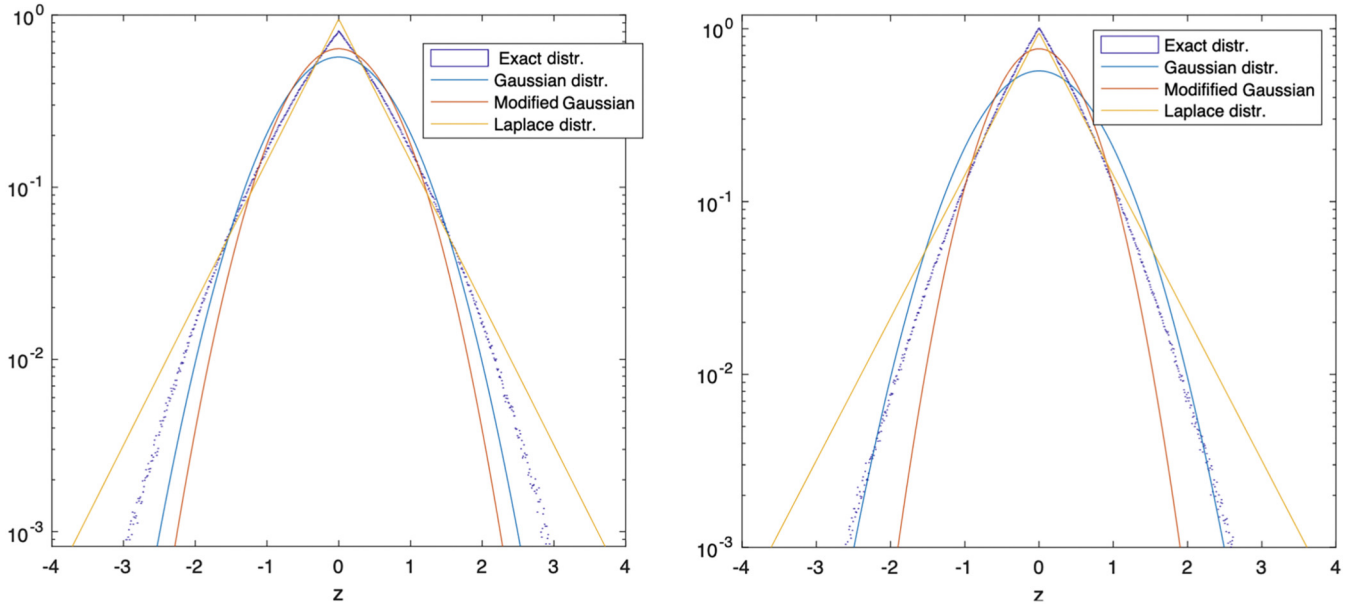

FIG. 13. Characterization of the random term $z(t)$. Comparison between Monte Carlo simulation (exact distribution), Laplace distribution, and two Gaussian distributions corresponding to $\alpha = 5/4$ and $\alpha = 1$, respectively. The latter refers to the *modified* case.

normally distributed with pdf $N(0, 1; \Gamma_y)$, using Eq. (B2), and following [76], we obtain a solution in terms of the Meijer G function,

$$p(z_1) = \int_{-1}^{1} \frac{p_x(\xi_x)}{|x|} N\left(0, 1; \frac{z_1}{x}\right) dx = \frac{1}{2\pi^2\sqrt{2}i} \int_{-i\infty}^{i\infty} \frac{\mathcal{G}[r]}{\mathcal{G}\left[r+\frac{3}{2}\right]} \left(\frac{z_1^2}{2}\right)^r dr, \tag{B3}$$

where $\mathcal{G}[r]$ is the standard Gamma function. With the use of (B3) we obtain a very simple result for the variance:

$$\sigma_{z_1}^2 = \int_{-\infty}^{\infty} z_1^2 p(z_1)\, dz_1 = \frac{1}{4}. \tag{B4}$$

After repeating the same computation for the second addend, $z_2(t) = \Gamma_x(t)\xi_y(t)$, we get

$$p(z_2) = \int_{-s}^{s} \frac{p_y(\xi_y)}{|y|} \mathcal{N}\left(\frac{z_2}{y}\right) dy = \frac{1}{2\pi^2\sqrt{2(1-e^2)}i} \int_{-i\infty}^{i\infty} \frac{\mathcal{G}[r]}{\mathcal{G}\left[r+\frac{3}{2}\right]} \left[\frac{z_2^2}{2(1-e^2)}\right]^r dr \tag{B5}$$

and

$$\sigma_{z_2}^2 = \frac{1-e^2}{4}. \tag{B6}$$

Unfortunately, a formula for the pdf of the whole signal $z = z_1 - z_2$ cannot be obtained in a closed form, since the convolution between the two pdfs does not allow an analytical solution. However, through a Monte Carlo simulation, it can be shown that $z(t)$ is almost distributed as a zero-mean Laplace distribution (see Fig. 13):

$$p_z(z) = \frac{1}{2m} e^{-\frac{|z|}{m}}, \tag{B7}$$

where $m = \langle |z| \rangle$ is the mean deviation. For our purposes, the above distribution can be approximated by a Gaussian one, having the variance of the real process z, that is provided by the sum of the variances of the two (independent) processes z_1 and z_2, namely,

$$\sigma_z^2 = \sigma_{z_1}^2 + \sigma_{z_2}^2 = \frac{1}{2} - \frac{e^2}{4}. \tag{B8}$$

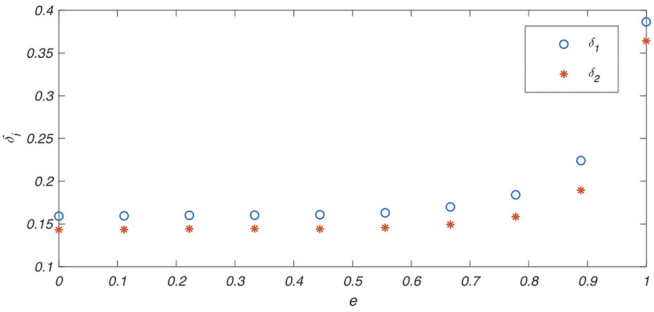

FIG. 14. Relative error between the Gaussian distribution and the exact one, according to the norm defined in Eq. (B10).

Figure 13 shows that even this latter approximation is quite reasonable. As $\sqrt{2D_\theta} = a\sigma_z\sqrt{2D_x/J}$, we conclude that the correct value of the parameter α appearing in the tensor $\boldsymbol{D}$ of Eq. (11) follows the remarkable relationship

$$\alpha = \frac{a^2\sigma_z^2}{J} = \frac{5}{2}\frac{1-\frac{e^2}{2}}{(2-e^2)} = \frac{5}{4}. \tag{B9}$$

Surprisingly, the above procedure justifies that tensor $\boldsymbol{D}$ is a constant diagonal matrix (with the last entry one-fourth exceeding the other two).

We have also verified that a Gaussian noise corresponding to $\alpha = 1$ (i.e., $\sigma_z^2 = J/a^2$) provides a better fit than the Gaussian one with the same variance as the actual one. This can be shown by computing the L_1 norm of the difference between the normal distributions $\mathcal{N}_i$ and the exact one $p(z)$, defined as

$$\delta_i = \frac{||p(z) - \mathcal{N}_i||_1}{||p(z)||_1} = \frac{\int dz[p(z) - \mathcal{N}_i]}{\int dz p(z)}, \tag{B10}$$

where $\mathcal{N}_1 = \mathcal{N}(0, 1/2 - e^2/4)$ and $\mathcal{N}_2 = \mathcal{N}(0, J/a^2)$.

The computation of δ_i is reported in Fig. 14. We see that for moderate values of eccentricity ($e < 0.8$) the relative error is quite small ($\delta_i < 0.2$), and the adoption of a Gaussian distribution which ensures $\alpha = 1$ provides lower errors than a Gaussian distribution having the same variance of the exact one.

All in all, for thermal reasons, α has a lower bound roughly equal to 5/4, for any eccentricity. Yet active particles may undergo biochemical processes that increase the rotational noise and more often lead to $\alpha \gg 1$.

[1] A. Morozov, From chaos to order in active fluids, Science **355**, 1262 (2017).

[2] C. Bechinger, R. Di Leonardo, H. Lowen, C. J. O. Reichhardt, G. Volpe, and G. Volpe, Active particles in complex and crowded environments, Rev. Mod. Phys. **88**, 045006 (2016).

[3] S. Heidenreich, J. Dunkel, S. H. L. Klapp, and M. Bär, Hydrodynamic length-scale selection in microswimmer suspensions, Phys. Rev. E **94**, 020601(R) (2016).

[4] A. M. Menzel, A. Saha, C. Hoell, and H. Löwen, Dynamical density functional theory for microswimmers, J. Chem. Phys. **144**, 024115 (2016).

[5] H. Reinken, S. H. L. Klapp, M. Bär, and S. Heidenreich, Derivation of a hydrodynamic theory for mesoscale dynamics in microswimmer suspensions, Phys. Rev. E **97**, 022613 (2018).

[6] C. Dombrowski, L. Cisneros, S. Chatkaew, R. E. Goldstein, and J. O. Kessler, Self-Concentration and Large-Scale Coherence in Bacterial Dynamics, Phys. Rev. Lett. **93**, 098103 (2004).

[7] I. Riedel, K. Kruse, and J. Howard, A self-organized vortex array of hydrodynamically entrained sperm cells, Science **309**, 300 (2005).

[8] N. S. Rossen, J. M. Tarp, J. Mathiesen, M. H. Jensen, and L. B. Oddershede, Long-range ordered vorticity patterns in living tissue induced by cell division, Nat. Commun. **5**, 5720 (2014).

[9] Y. Sumino, K. H. Nagai, Y. Shitaka, D. Tanaka, K. Yoshikawa, H. Chaté, and K. Oiwa, Large-scale vortex lattice emerging from collectively moving microtubules, Nature (London) **483**, 448 (2012).

[10] A. Doostmohammadi, J. Ignés-Mullol, J. M. Yeomans, and F. Sagués, Active nematics, Nat. Commun. **9**, 3246 (2018).

[11] M. C. Marchetti, J. F. Joanny, S. Ramaswamy, T. B. Liverpool, J. Prost, M. Rao, and R. A. Simha, Hydrodynamics of soft active matter, Rev. Mod. Phys. **85**, 1143 (2013).

[12] H. Löwen, Inertial effects of self-propelled particles: From active Brownian to active Langevin motion, J. Chem. Phys. **152**, 040901 (2020).

[13] J. R. Howse, R. A. L. Jones, A. J. Ryan, T. Gough, R. Vafabakhsh, and R. Golestanian, Self-Motile Colloidal Particles: From Directed Propulsion to Random Walk, Phys. Rev. Lett. **99**, 048102 (2007).

[14] B. Hagen, S. van Teeffelen, and H. Löwen, Brownian motion of a self-propelled particle, J. Phys.: Condens. Matter **23**, 194119 (2011).

[15] F. Kümmel, B. ten Hagen, R. Wittkowski, I. Buttinoni, R. Eichhorn, G. Volpe, H. Löwen, and C. Bechinger, Circular Motion of Asymmetric Self-Propelling Particles, Phys. Rev. Lett. **110**, 198302 (2013).

[16] C. Kurzthaler, C. Devailly, J. Arlt, T. Franosch, W. C. K. Poon, V. A. Martinez, and A. T. Brown, Probing the Spatiotemporal Dynamics of Catalytic Janus Particles with Single-Particle Tracking and Differential Dynamic Microscopy, Phys. Rev. Lett. **121**, 078001 (2018).

[17] C. Scholz, M. Engel, and T. Pöschel, Rotating robots move collectively and self-organize, Nat. Commun. **9**, 931 (2018).

[18] L. Caprini, C. Maggi, and U. Marini Bettolo Marconi, Collective effects in confined active Brownian particles, J. Chem. Phys. **154**, 244901 (2021).

[19] G. E. Morfill and A. V. Ivlev, Complex plasmas: An interdisciplinary research field, Rev. Mod. Phys. **81**, 1353 (2009).

[20] V. Narayan, S. Ramaswamy, and N. Menon, Long-lived giant number fluctuations in a swarming granular nematic, Science **317**, 105 (2007).

[21] C. A. Weber, T. Hanke, J. Deseigne, S. Léonard, O. Dauchot, E. Frey, and H. Chaté, Long-Range Ordering of Vibrated Polar Disks, Phys. Rev. Lett. **110**, 208001 (2013).

[22] A. Deblais, T. Barois, T. Guerin, P. H. Delville, R. Vaudaine, J. S. Lintuvuori, J. F. Boudet, J. C. Baret, and H. Kellay, Boundaries Control Collective Dynamics of Inertial Self-Propelled Robots, Phys. Rev. Lett. **120**, 188002 (2018).

[23] A. Kudrolli, G. Lumay, D. Volfson, and L. S. Tsimring, Swarming and Swirling in Self-Propelled Polar Granular Rods, Phys. Rev. Lett. **100**, 058001 (2008).

[24] J. Deseigne, O. Dauchot, and H. Chaté, Collective Motion of Vibrated Polar Disks, Phys. Rev. Lett. **105**, 098001 (2010).

[25] G. A. Patterson, P. I. Fierens, F. Sangiuliano Jimka, P. G. König, A. Garcimartín, I. Zuriguel, L. A. Pugnaloni, and D. R. Parisi, Clogging Transition of Vibration-Driven Vehicles Passing through Constrictions, Phys. Rev. Lett. **119**, 248301 (2017).

[26] G. Junot, G. Briand, R. Ledesma-Alonso, and O. Dauchot, Active versus Passive Hard Disks against a Membrane: Mechanical Pressure and Instability, Phys. Rev. Lett. **119**, 028002 (2017).

[27] G. Notomista, S. Mayya, A. Mazumdar, S. Hutchinson, and M. Egerstedt, A study of a class of vibration-driven robots: Modeling, analysis, control and design of the brushbot, in *2019 IEEE/RSJ International Conference on Intelligent Robots and Systems (IROS)* (IEEE, 2019), pp. 5101–5106.

[28] S. Mayya, G. Notomista, D. Shell, S. Hutchinson, and M. Egerstedt, Achieving non-uniform densities in vibration driven robot swarms using phase separation theory, arXiv:1902.10662.

[29] O. Dauchot and V. Démery, Dynamics of a Self-Propelled Particle in a Harmonic Trap, Phys. Rev. Lett. **122**, 068002 (2019).

[30] M. Mijalkov and G. Volpe, Sorting of chiral microswimmers, Soft Matter **9**, 6376 (2013).

[31] M. Leyman, F. Ogemark, J. Wehr, and G. Volpe, Tuning phototactic robots with sensorial delays, Phys. Rev. E **98**, 052606 (2018).

[32] D. Klotsa, As above, so below, and also in between: Mesoscale active matter in fluids, Soft Matter **15**, 8946 (2019).

[33] H. Mukundarajan, T. C. Bardon, D. H. Kim, and M. Prakash, Surface tension dominates insect flight on fluid interfaces, J. Exp. Biol. **219**, 752 (2016).

[34] J. Rabault, R. A. Fauli, and A. Carlson, Curving to Fly: Synthetic Adaptation Unveils Optimal Flight Performance of Whirling Fruits, Phys. Rev. Lett. **122**, 024501 (2019).

[35] H.-W. Huang, F. E. Uslu, P. Katsamba, E. Lauga, M. S. Sakar, and B. J. Nelson, Adaptive locomotion of artificial microswimmers, Sci. Adv. **5**, eaau1532 (2019).

[36] P. Degen, Self-propelling capsules as artificial microswimmers, Curr. Opin. Colloid Interface Sci. **19**, 611 (2014).

[37] A. S. Rzhevskiy, T. R. R. Singh, R. F. Donnelly, and Y. G. Anissimov, Microneedles as the technique of drug delivery enhancement in diverse organs and tissues, J. Control. Release **270**, 184 (2018).

[38] Y. Couder and E. Fort, Single-Particle Diffraction and Interference at a Macroscopic Scale, Phys. Rev. Lett. **97**, 154101 (2006).

[39] R. N. Valani, A. C. Slim, and T. Simula, Superwalking Droplets, Phys. Rev. Lett. **123**, 024503 (2019).

[40] D. Helbing, Traffic and related self-driven many-particle systems, Rev. Mod. Phys. **73**, 1067 (2001).

[41] J. Zhang, W. Mehner, E. Andresen, S. Holl, M. Boltes, A. Schadschneider, and A. Seyfried, Comparative analysis of pedestrian, bicycle and car traffic moving in circuits, Procedia: Social Behav. Sci. **104**, 1130 (2013).

[42] D. Chowdhury, L. Santen, and A. Schadschneider, Statistical physics of vehicular traffic and some related systems, Phys. Rep. **329**, 199 (2000).

[43] A. Nakayama, M. Kikuchi, A. Shibata, Y. Sugiyama, S. ichi Tadaki, and S. Yukawa, Quantitative explanation of circuit experiments and real traffic using the optimal velocity model, New J. Phys. **18**, 043040 (2016).

[44] A. P. Solon, Y. Fily, A. Baskaran, M. E. Cates, Y. Kafri, M. Kardar, and J. Tailleur, Pressure is not a state function for generic active fluids, Nat. Phys. **11**, 673 (2015).

[45] C. Scholz, S. Jahanshahi, A. Ldov, and H. Löwen, Inertial delay of self-propelled particles, Nat. Commun. **9**, 5156 (2018).

[46] H. H. Wensink and H. Löwen, Aggregation of self-propelled colloidal rods near confining walls, Phys. Rev. E **78**, 031409 (2008).

[47] U. Marini Bettolo Marconi, A. Sarracino, C. Maggi, and A. Puglisi, Self-propulsion against a moving membrane: Enhanced accumulation and drag force, Phys. Rev. E **96**, 032601 (2017).

[48] A. Baskaran and M. C. Marchetti, Enhanced Diffusion and Ordering of Self-Propelled Rods, Phys. Rev. Lett. **101**, 268101 (2008).
[49] M. Enculescu and H. Stark, Active Colloidal Suspensions Exhibit Polar Order under Gravity, Phys. Rev. Lett. **107**, 058301 (2011).
[50] S. C. Takatori and J. F. Brady, Inertial effects on the stress generation of active fluids, Phys. Rev. Fluids **2**, 094305 (2017).
[51] S. Shankar and M. C. Marchetti, Hidden entropy production and work fluctuations in an ideal active gas, Phys. Rev. E **98**, 020604(R) (2018).
[52] A. Manacorda and A. Puglisi, Lattice Model to Derive the Fluctuating Hydrodynamics of Active Particles with Inertia, Phys. Rev. Lett. **119**, 208003 (2017).
[53] H. D. Vuijk, J. U. Sommer, H. Merlitz, J. M. Brader, and A. Sharma, Lorentz forces induce inhomogeneity and flux in active systems, Phys. Rev. Res. **2**, 013320 (2020).
[54] I. Abdoli, H. D. Vuijk, J. U. Sommer, J. M. Brader, and A. Sharma, Nondiffusive fluxes in a Brownian system with Lorentz force, Phys. Rev. E **101**, 012120 (2020).
[55] Z. Mokhtari, T. Aspelmeier, and A. Zippelius, Collective rotations of active particles interacting with obstacles, Europhys. Lett. **120**, 14001 (2017).
[56] J. Um, T. Song, and J.-H. Jeon, Langevin dynamics driven by a telegraphic active noise, Front. Phys. **7**, 143 (2019).
[57] S. Das, G. Gompper, and R. G. Winkler, Local stress and pressure in an inhomogeneous system of spherical active Brownian particles, Sci. Rep. **9**, 6608 (2019).
[58] A. Bodrova, A. Chechkin, A. Cherstvy, H. Safdari, M. Sokolov, and R. Metzler, Underdamped scaled Brownian motion: (Non-)existence of the overdamped limit in anomalous diffusion, Sci. Rep. **6**, 30520 (2016).
[59] G. J. Hancock and M. H. A. Newman, The self-propulsion of microscopic organisms through liquids, Proc. R. Soc. A: Math. Phys. Eng. Sci. **217**, 96 (1953).
[60] J. Happel and H. Brenner, *Low Reynolds Number Hydrodynamics: With Special Applications to Particulate Media*, Prentice-Hall International Series in the Physical and Chemical Engineering Sciences (Prentice-Hall, New York, 1965).
[61] A. T. Chwang and T. Y.-T. Wu, Hydromechanics of low-Reynolds-number flow. Part 2. Singularity method for Stokes flows, J. Fluid Mech. **67**, 787 (1975).
[62] C. Pozrikidis, *Introduction to Theoretical and Computational Fluid Dynamics* (Oxford University Press, New York, 2011).
[63] L. Caprini, A. Puglisi, and A. Sarracino, Fluctuation–dissipation relations in active matter systems, Symmetry **13**, 81 (2021).
[64] A. Sarracino and A. Vulpiani, On the fluctuation-dissipation relation in non-equilibrium and non-Hamiltonian systems, Chaos **29**, 083132 (2019).
[65] J.-P. Duroudier, Mechanics and thermics of gaseous fluidized beds, *Divided Solids Mechanics*, Chap. 6 (Elsevier, 2016), pp. 223–259.
[66] M. Mandø and L. Rosendahl, On the motion of non-spherical particles at high Reynolds number, Powder Technol. **202**, 1 (2010).
[67] S. R. De Groot and P. Mazur, *Non-equilibrium Thermodynamics*, Dover Books on Physics (Dover Publications, Mineola, NY, 2003).
[68] G. Gallavotti, *Nonequilibrium and Irreversibility*, Theoretical and Mathematical Physics (Springer, Cham, 2014).
[69] M. Friedlin and A. Wentzell, *Random Perturbations of Dynamical Systems*, Grundlehren der mathematischen Wissenschaften (Springer, Berlin, 2012).
[70] A. Suma, G. Gonnella, D. Marenduzzo, and E. Orlandini, Motility-induced phase separation in an active dumbbell fluid, Europhys. Lett. **108**, 56004 (2014).
[71] L. F. Cugliandolo, P. Digregorio, G. Gonnella, and A. Suma, Phase Coexistence in Two-Dimensional Passive and Active Dumbbell Systems, Phys. Rev. Lett. **119**, 268002 (2017).
[72] P. Cremer and H. Löwen, Scaling of cluster growth for coagulating active particles, Phys. Rev. E **89**, 022307 (2014).
[73] P. Singh and A. Kundu, Crossover behaviours exhibited by fluctuations and correlations in a chain of active particles, J. Phys. A: Math. Theor. **54**, 305001 (2021).
[74] L. F. Cugliandolo, G. Gonnella, and A. Suma, Rotational and translational diffusion in an interacting active dumbbell system, Phys. Rev. E **91**, 062124 (2015).
[75] C. Camporeale, Mesoscopic theory of active matter, Università di Torino (2019).
[76] G. Grimmett and D. Stirzaker, *Probability and Random Processes* (Oxford University Press, Oxford, 2020).